PHYSICAL REVIEW E VOLUME 53, NUMBER 6 JUNE 1996

Dynamics of two-dimensional traveling-wave convection patterns

A. La Porta and C. M. Surko
Department of Physics, University of California, San Diego, La Jolla, California 92093

(Received 10 October 1995)

We report an experimental study of traveling-wave convection patterns in a binary mixture of ethanol and water. We survey the patterns observed in a large aspect ratio cylindrical container over a broad range of Rayleigh numbers. It is found that disordered patterns observed immediately after traveling-wave convection is initiated evolve toward organized multidomain patterns and that the nature of the multidomain patterns depends on the Rayleigh number. A numerical algorithm for extracting the complex order parameter from traveling-wave patterns and measuring their dynamical properties is described. This technique is used to characterize the dynamic aspects of traveling-wave convection patterns observed near the saddle node bifurcation. It is shown that the instantaneous rate of deformation of the pattern can be determined, and use of this information as a point of comparison with model equations is discussed. The joint wave number, frequency distribution for traveling-wave patterns is calculated and is shown to be significantly different from the dispersion curves previously obtained from one-dimensional traveling-wave convection patterns. [S1063-651X(96)07705-7]

PACS number(s): 47.54.+r, 47.55.Hd, 47.27.Te

I. INTRODUCTION

Rayleigh-Bénard convection is perhaps the most widely studied example of a nonequilibrium pattern-forming system arising from a finite wave number instability because the underlying physical mechanisms are well understood, the experimental conditions can be precisely controlled, and a great variety of phenomena can be observed [1]. Convection in pure fluids, not driven too far beyond the onset of convection, is amenable to theoretical analysis, and a fairly satisfactory understanding of pattern forming issues has been achieved. In this case, the instabilities are stationary and to some approximation the pattern evolves toward an optimum configuration [2]. This relaxational character of pure fluid convection patterns is reflected in the fact that the model equation that is most frequently applied to this regime of convection, the Swift-Hohenberg equation, has a Lyaponov functional that decreases with time. This functional can be interpreted as an effective free energy that is minimized for a stable pattern [3]. Departures from this relaxational paradigm are observed under special circumstances. For instance, it has been found that in cases where the boundary conditions are inconsistent with the preferred straight roll configuration, persistent time dependence of the pattern can occur [4,5]. Intrinsic instabilities of the patterns, or intensely chaotic behavior, such as spiral chaos, is generally observed only at higher Rayleigh number, especially in low Prandtl number or non-Boussinesq fluids [6–8].

The situation for convection in a binary mixture of ethanol and water is very different. Over a wide range of parameters, the onset of convection is a subcritical Hopf bifurcation to a state of oscillatory convection [9]. Near onset, the weakly nonlinear oscillatory convection can exhibit chaotic dynamics, including repeated growth and collapse of the convective amplitude [10,11], dispersive chaos [12], and formation of localized states in one or two dimensions [13–16]. If the Rayleigh number is set above the onset value, the oscillatory convection grows in amplitude until it reaches a strongly nonlinear state of continuously overturning convection in which the rolls propagate slowly with a well defined phase velocity [17]. We refer to this state as traveling-wave (TW) convection.

In one-dimensional geometries, the TW state exhibits some of the same behavior that characterizes the weakly nonlinear state, such as wave number instabilities [18] and confined states of convection [19]. In two dimensions, traveling-wave convection patterns typically consist of several competing domains of traveling waves propagating in different directions. In contrast to the case of stationary convection, the dynamics of the traveling-wave patterns are not relaxational and the point defects that are important in stationary convection patterns give way to slowly moving domain walls between competing patches of traveling waves. The model equations that are usually applied to this system, such as complex generalizations of the Swift-Hohenberg equation, are not relaxational [20,21].

In this paper, we describe an investigation of traveling-wave convection patterns in a container with a large aspect ratio. We describe disordered patterns in which most of the area of the pattern evolves independently of the cell boundary, as well as ordered multidomain patterns in which the geometry of the cell boundary is a stronger influence. We present a survey of the traveling-wave convection patterns observed over a broad range of Rayleigh numbers and we describe an analysis technique that allows us to obtain the complex order parameter from the experimental convection patterns. This approach allows us to obtain all of the important dynamical properties of the pattern and it is suitable for direct comparison with model equations. Finally, we make use of this technique to give a detailed treatment of the dynamical properties of traveling-wave convection patterns at low Rayleigh number.

II. BINARY FLUID CONVECTION

In Rayleigh-Bénard convection, a thin layer of fluid, confined between two flat thermally conducting plates, is heated from below so that a fixed temperature difference ΔT is maintained between the upper and lower boundaries. For the usual case of positive thermal expansion coefficient, an unstable density gradient develops as the temperature difference is increased and the fluid layer becomes unstable to a convective flow, which results in enhanced heat transport. The onset of convection involves the interplay of buoyancy, viscous damping, and thermal diffusion and is determined by the Rayleigh number

$$\mathrm{Ra}=\frac{\alpha g h^3 \Delta T}{\kappa \nu}, \tag{1}$$

where h is the cell height, α is the thermal expansion coefficient, g is the acceleration of gravity, κ is the thermal diffusion constant, and ν is the viscosity [22]. In the following sections we will refer to the reduced Rayleigh number $r=\mathrm{Ra}/1708$, which is normalized by the onset Rayleigh number of an infinitely wide layer of pure fluid. It is also necessary to specify the Prandtl number

$$\mathrm{Pr}=\frac{\nu}{\kappa}, \tag{2}$$

which determines the onset of secondary instabilities and influences the nature of convection patterns.

The binary fluid system falls into the class of double-diffusive convection systems in which there are two buoyant species, in this case heat and solute, which diffuse through the liquid and are advected by the velocity field. In systems where two buoyant species diffuse independently, such as double diffusive convection of two solutes [23], the system is described by two independent forcing parameters corresponding to the applied concentration gradients of the two species. In the ethanol-water system, the boundaries are impermeable to both components of the fluid and a concentration gradient cannot be externally imposed. Instead, an ethanol concentration gradient is driven by the temperature gradient and the system is described by a single forcing parameter, the Rayleigh number, and a coupling between the temperature and concentration fields. The transport of ethanol in the fluid is governed by

$$\mathbf{j}_c=-D_c\nabla c+D_c S_t c(1-c)\nabla T+\mathbf{u}c, \tag{3}$$

where $\mathbf{j}_c$ is the ethanol flux, D_c is the mass diffusion coefficient, c is the concentration of ethanol, $\mathbf{u}$ is the velocity field, and S_t is the Soret coefficient [24]. The first and third terms on the right-hand side are the ordinary diffusion and advection terms, but the term proportional to S_t indicates that an ethanol flux arises from a temperature gradient, which, in our case, drives ethanol toward the colder regions of the cell. The corresponding term in the heat transport equation, in which a heat current is driven by the concentration gradient (the Dufour effect), is negligible in ethanol-water mixtures.

Two additional parameters are required to describe the binary fluid system. The separation ratio is the temperature-concentration coupling parameter and is defined by

$$\psi=-c(1-c)S_t\frac{\beta}{\alpha}, \tag{4}$$

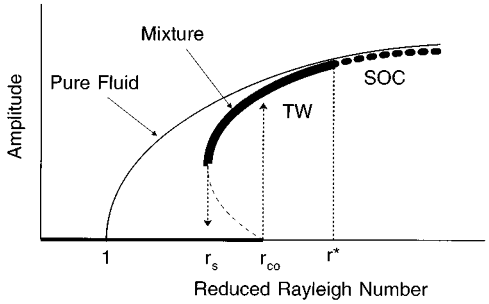

FIG. 1. Schematic bifurcation diagram for convection in a pure fluid and in a binary mixture with negative separation ratio. In the mixture, the heavy solid line indicates traveling-wave (TW) convection and the heavy dashed line indicates stationary overturning convection (SOC).

where β is the concentration expansion coefficient. The separation ratio indicates the extent to which the density of the fluid is stratified by the concentration field arising from the imposed temperature difference. In the present experiment, ψ is negative, indicating that the density gradient associated with the concentration field opposes the thermal density gradient and tends to stabilize the fluid layer against the onset of thermal convection. The Lewis number

$$\mathcal{L}=\frac{D_c}{\kappa}, \tag{5}$$

where D_c and κ are the mass and thermal diffusion coefficients, gives the ratio of the time scales associated with mass diffusion and thermal diffusion. The onset of convection is oscillatory for small $\mathcal{L}$ and for sufficiently negative values of ψ [26].

The Lewis number for ethanol-water mixtures is approximately 10^{-2}, so that concentration fluctuations are much longer lived than thermal fluctuations. For this strong separation of time scales, an oscillatory onset of convection is observed for all measurable $\psi<0$. The experiments described below are performed with a mixture of 8% ethanol (by weight) in water at an average temperature of 26 °C. This mixture has a Prandtl number of 10.5, which is roughly twice that of water at the same temperature, and has a separation ratio of -0.24, which is the largest negative value possible at this temperature [25].

A schematic representation of the bifurcation diagram is shown in Fig. 1. The large negative separation ratio of the 8% ethanol mixture leads to a strong suppression of the onset of convection r_{co}. The onset is strongly subcritical, and above r_{co}, convection quickly grows to a large amplitude TW state that is stable over a broad range of Rayleigh numbers. As r is increased further above r_{co}, the TW phase velocity decreases, becoming zero at $r^\star$, where a transition to stationary overturning convection occurs [27]. When the system is in the TW state and r is decreased below r_{co}, the TW velocity increases until a saddle node bifurcation is reached at r_s and the finite amplitude convection state abruptly disappears. In the experiments described below, the measured values for the transition Rayleigh numbers are $r_{\mathrm{co}}=1.40$, $r^\star=1.58$, and $r_s=1.23$, so that traveling-wave

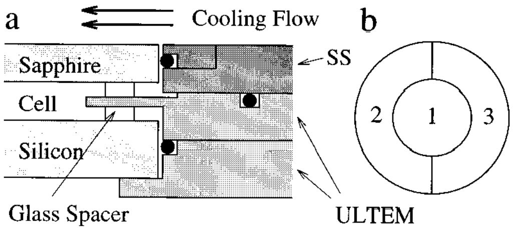

FIG. 2. (a) Schematic diagram of the convection cell seals and boundary configuration. (b) Three segments of the film resistor used to heat the bottom plate.

convection can be observed for $1.23<r<1.58$. The temperature difference at onset is approximately 1.7°C and the Boussinesq approximation is valid. The relevant fluid parameters are $\alpha=3.19\times10^{-4}$ K^{-1}, $\kappa=1.29\times10^{-3}$ cm^2/sec, and $\nu=1.18\times10^{-2}$ cm^2/sec.

The data shown below are normalized to the characteristic time and distance scales in the system. Distances are normalized to the cell height $h=0.4$ cm, which sets the width of a convection roll, and time intervals and frequencies are expressed in terms of the vertical thermal diffusion time $\tau_\kappa\equiv h^2/\kappa=124$ sec. This is the most important time scale in the system, although the dynamical properties can also have a weak dependence on the Prandtl number. Other interesting time scales are the vertical viscous dissipation time $\tau_\nu\equiv h^2/\nu=11.8$ sec and the vertical mass diffusion time $\tau_c\equiv h^2/D_c\approx12\,000$ sec. The measured period of the Hopf bifurcation is $\tau_H\approx75$ sec and the measured period of the traveling-wave state at the saddle node is $\tau_s\approx210$ sec.

III. APPARATUS

The convection cell used for the experiments described below is a standard design consisting of an electrically heated bottom plate and a sapphire top plate that is cooled by a temperature regulated water flow bath. A window in the flow channel provides optical access for visualization of the convection cell through the bath. The cylindrical convection container has a diameter of 21 cm and a height of 0.4 cm, giving an aspect ratio $(\Gamma=r/h)$ of 26.

For the bottom plate, we have adopted the polished silicon mirror employed in convection experiments by Kolodner [28]. The experiment described here uses a 1.91-cm-thick polycrystalline silicon disk that is mirror polished to a flatness of one wavelength per inch. The thermal conductivity of the silicon plate is 1.5W/cm K, which is a factor of 2.5 smaller than copper, and the reflectivity of silicon is somewhat low at ~60%. However, silicon has several advantages over the more commonly used plated copper mirrors, which, in our view, override the disadvantages. Silicon does not react with water and requires no coating. Although silicon is brittle, it is very hard and plastic deformation of the mirror is negligible. In contrast to rhodium or gold-coated copper mirrors, which have been used in past experiments, we have found no degradation of the mirrored surface after more than one year's exposure to the working fluid.

The configuration of the convection cell is represented schematically in Fig. 2(a). The upper boundary of the cell is a single-crystal sapphire disk of thickness 1.02 cm, which is also polished to flatness of 1 wavelength per inch. The separation of the top and bottom plates is set by 12 finely ground glass spacers and the uniformity of spacing between the upper and lower cell boundaries is measured by interferometry using a helium-neon laser. The uniformity of spacing is approximately one wavelength per inch. The working fluid is confined by an o-ring seal between the side surface of the sapphire and the stainless steel flow channel and by an o-ring seal between the side of the silicon plate and an ULTEM plastic holder, which is bolted and o-ring sealed to the underside of the flow bath. Fluid is introduced into the convection cell through holes in the upper part of the bottom plate holder. ULTEM was chosen for mounting the bottom plate because it has acceptable mechanical properties, good chemical stability, and a low thermal conductivity, which minimizes heat leaks between the top and bottom plates. The boundary of the cell is a 0.3-cm-thick fin that is machined as an integral part of the ULTEM bottom plate holder, providing an unforced boundary condition.

The convection cell is positioned so that the sapphire top plate is flush with the flow channel and the flow of cooling water over the cell is not disrupted. During assembly and filling of the cell, the upper plate is held against the lower plate by a rubber gasket pressed under a stainless steel ring, but this is removed after the cell is filled. During experiments the sapphire is held in place by the compressed o ring and the pressure in the flow channel above. The cell is filled by evacuating the convection cell using a mechanical vacuum pump and allowing the degassed ethanol-water mixture to be drawn into the evacuated volume. Thermal expansion of the convecting fluid is accommodated by a small stainless steel expansion bellows coupled to the fluid volume.

The main technical difficulty in this experiment is maintaining a constant and uniform Rayleigh number across the large convection cell. Uniform heating of the bottom plate is achieved using an array of film heaters, as shown in Fig. 2(b). The heaters are connected in parallel and nominally configured for uniform heat delivery, but variable shunt resistors are installed on the individual segments to make small corrections as described below. Achieving uniform cooling of the top plate by the flow bath is more difficult in view of the rather large area of the convection cell and because of the large heat flux, which can reach 50 W for typical experimental conditions.

A technique frequently used with cylindrical convection cells is to install a flow manifold or array of jets, so that water rushes in from around the edge of the convection cell and flows toward the center, before making its way to an exhaust manifold. This arrangement was used in a preliminary version of our experiment, but it was found that more uniform cooling could be achieved using a linear channel flow across the top plate. In both configurations there are two main problems. The first is that the temperature of the cooling water increases as it flows over the convection cell and collects heat. The second and, in our experience, the more severe problem is that the cell is less efficiently cooled where the flow is less vigorous or where closed eddies form. In the case of the circularly symmetric flow there is inevitably a turbulent stagnation point over the center of the cell and the detailed flow is very complex and difficult to characterize. In contrast, the linear channel flow is simple and relatively ef-

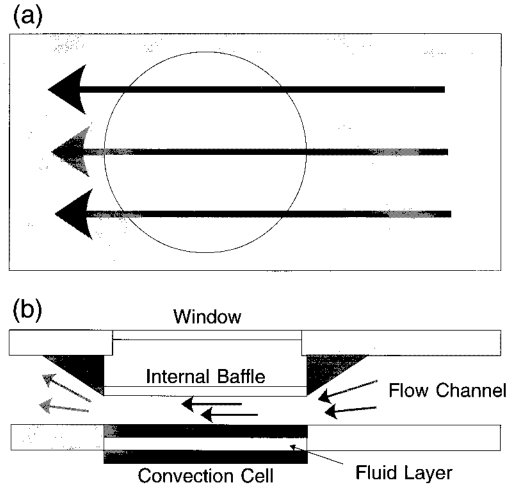

FIG. 3. Schematic diagrams of the cooling flow channel above the convection cell; (a) above view and (b) cross-sectional view.

ficient in transporting heat away from the convection cell.

The linear flow channel, shown in Fig. 3, is designed to have a high Reynolds number where the flow passes over the convection cell. Water enters the channel through eight 0.5-in.-diam pipes that are fed by two 38 liter/min magnetically coupled pumps, each of which feeds four inlets to the flow channel. After flowing 24 cm along the 3.2-cm-high, 30-cm-wide channel, the flow is confined to a 0.7-cm-high channel by an internal baffle as it passes over the convection cell. By repositioning the baffle, the geometry of the channel can be varied without requiring significant modification of the flow channel. The Reynolds number for the channel flow above the convection cell is estimated to be $\gtrsim 2\times 10^4$. Turbulence in this relatively high Reynolds number flow causes intense vertical mixing in the fluid that efficiently moves heated water away from the upper surface of the convection cell.

In order to measure the temperature uniformity, the convection cell was partitioned into seven identical subcells by placing seven glass rings having a height of 0.375 cm and an inner diameter of 3.8 cm in the convection container. Six of the subcells were placed around the perimeter and one was placed at the center of the main convection cell. By slowly increasing the Rayleigh number above $r_{\rm co}$ and watching the onset of convection in the individual subcells, we could measure the nonuniformity in the temperature difference with a sensitivity of about 1 mK. An important advantage of this technique is that it directly measures the Rayleigh number in the convection cell itself and includes all effects that influence the experiment, such as nonuniformities in heating or cooling and heat leaks to the room or between different components of the apparatus.

When uniform heating was applied to the bottom plate, we found that the temperature difference across the fluid layer was approximately 30 mK larger at the center of the cell than at the edges. Since the linear flow of cooling water across the top of the convection cell cannot produce a radial temperature gradient on the top plate, our interpretation is that a small heat leak from the bottom plate to the flow bath through the mounting hardware created a nonuniform temperature distribution on the bottom plate. This temperature inhomogeneity was eliminated by reducing the heating power of sector 1 of the heater [see Fig. 2(b)] by approximately 5%. (Because of the high thermal conductivity of the silicon bottom plate, the effect on the fluid layer is much smaller.) After this correction was applied, a 12-mK temperature difference between the areas corresponding to the leading edge and the trailing edge of the cooling flow was observed. This nonuniformity was suppressed by increasing the heat flux to sector 3 of the heater, which corresponds to the trailing edge of the cooling flow, by approximately 0.5%. After this compensation was applied, no nonuniformity was observed. To summarize, we measured a 12-mK peak-to-peak variation in the absolute temperature distribution on the top plate of the cell, corresponding to a 0.7% variation in the Rayleigh number at onset. By matching the bottom plate temperature distribution to the top plate distribution, we estimate that the variation in the Rayleigh number was reduced by at least a factor of 4, so that the data presented below were taken with an 0.2% p.-p. variation in Rayleigh number at onset.

The top plate temperature is held constant by a PolyScience programmable circulating flow bath and monitored by thermistors in the flow channel. The bottom temperature is controlled by a servo-loop based on an ac resistance bridge that is sensitive to the resistance of a thermistor embedded in the bottom plate. The reference for the ac bridge is provided by a six digit computer controlled variable ratio transformer, which is used for computer control of the Rayleigh number. Using a combination of analog feedback and computer servo control, the fluctuation in the Rayleigh number is approximately 2-mK rms.

The patterns are visualized by white light shadowgraph. The large aperture of the cell makes the typical refracting-optic shadowgraph configuration inconvenient. Instead, a reflecting optic design is used that employs a parabolic reflector having a 2 m focal length as the main focusing element [29]. Numerical simulations of the system and calibrations indicate that the distortions of the image are less than 1%.

The experiment is controlled using a *C* language computer program that executes predefined temperature protocols, which may be modified during the course of a run. The images are recorded using a Sony model SSC-M370 charge coupled device camera and digitized to eight-bit resolution using a personal computer frame grabber. A Sony EVT-820 time lapse video cassette recorder is also used to monitor the long-term evolution of patterns. The process control program displays the status of the experiment, including the current image, temperatures, Rayleigh number, and protocol status. The images, along with associated temperature data, are stored in binary computer files for further analysis on a UNIX work station, as described below.

IV. SURVEY OF TRAVELING-WAVE PATTERNS

While traveling-wave convection patterns have been observed and studied in previous experiments on convection in ethanol-water mixtures, these experiments had a smaller aspect ratio than the present experiment and the patterns observed were strongly influenced by the system boundary [9,16]. As discussed below, in the larger aspect ratio system disordered states consisting of many small domains of traveling waves can be created in which a significant fraction of

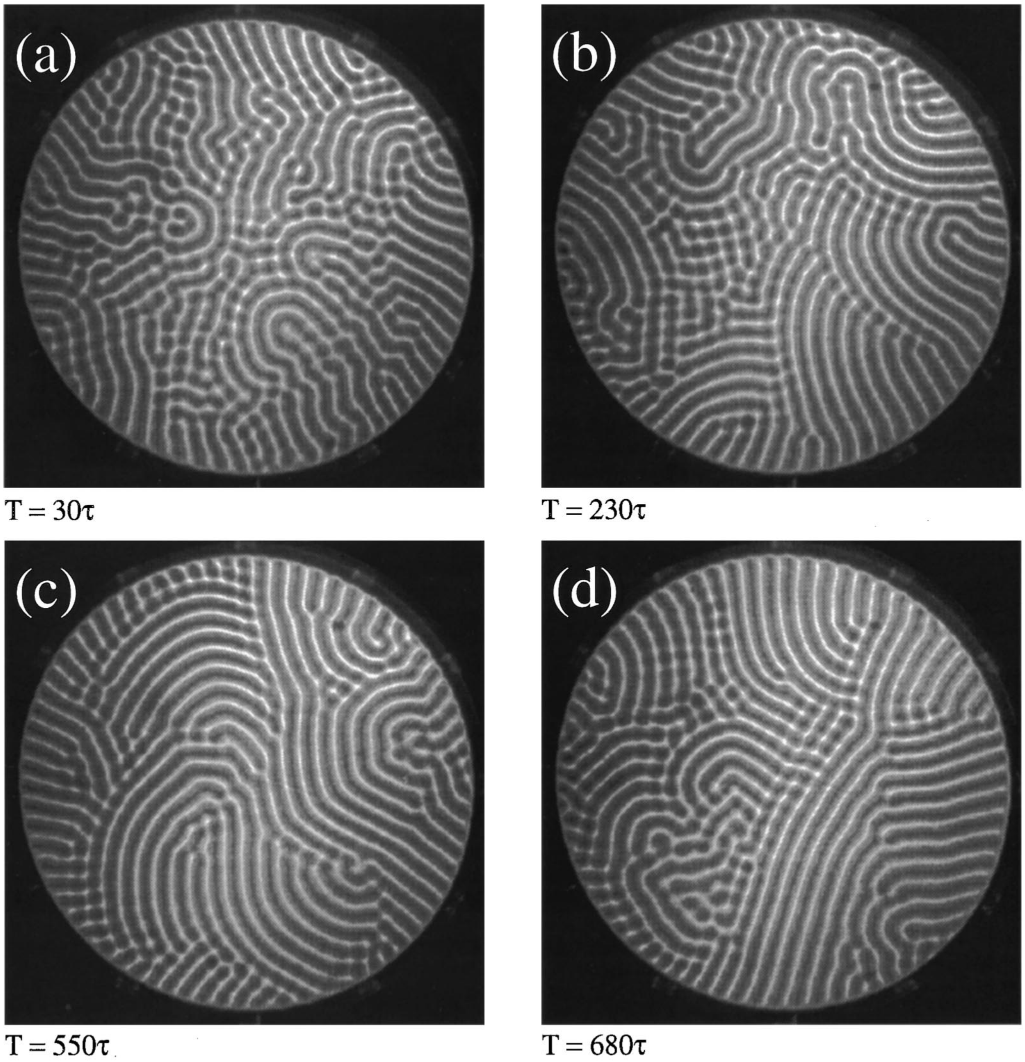

FIG. 4. Raw images of disordered convection patterns observed in the 21-cm-diam convection cell after a sudden decrease from $r = 1.9$ to $r = 1.28$: (a) after $30\tau_\kappa$, (b) after $230\tau_\kappa$, (c) after $550\tau_\kappa$, and (d) after $680\tau_\kappa$, where τ_κ is the characteristic vertical thermal diffusion time of 124 sec.

the area of the pattern does not appear to interact with the cell boundary. Over time, the size of the domains increases until the mean domain size is of the order of the size of the container and the boundaries again become a significant influence. In this latter regime, the patterns typically consist of three or four domains of traveling waves, separated by well defined domain boundaries, and it is the dynamics of these domain boundaries that appears to control the evolution of the patterns.

A. Disordered states

Traveling-wave convection patterns may be created using a variety of protocols, all of which lead to disordered initial states. When r is slowly raised above the onset value r_{co}, small amplitude oscillatory convection is first observed. As the convection amplitude grows the oscillation frequency decreases from the Hopf frequency to the traveling-wave frequency and the pattern breaks up into small patches of large amplitude traveling waves that quickly fill the convection cell. An alternate protocol is to set r above $r^\star$ and allow a stationary convection pattern to develop, before setting r to a value on the traveling-wave branch. When r is reduced to a value below $r^\star$, the stationary convection rolls begin moving in one direction or another and again small patches of traveling waves are created. In either case, after about $30\tau_\kappa$ (where τ_κ is the characteristic vertical thermal diffusion time of 124 sec) the pattern evolves to a state of spatiotemporal disorder whose character depends on the Rayleigh number but is not very sensitive to the method by which the state was initiated. In general, the disorder is most intense for Rayleigh numbers near r_s, where the traveling-wave velocity is highest, and less intense at higher values of the Rayleigh number.

Figure 4 shows an example of the evolution of a disordered state, created by a sudden decrease of Rayleigh number from 1.9 to 1.28, a value just above r_s, where the most disordered patterns occur. Figure 4(a) shows the pattern $30\tau_\kappa$ after the change of Rayleigh number, when the spatiotemporal disorder is at its maximum. The pattern is composed of small patches of traveling waves, what we might characterize as ''billowing structures'' (visible in the figure as semicircular arches) and cross-roll patches, in which a small area of the pattern alternates between two mutually orthogonal sets of standing waves at a frequency slightly lower than the traveling-wave frequency. The convection rolls tend to be aligned perpendicular to the unforced boundary of the cell and this seems to impose some order on the peripheral regions of the pattern, so that the most intense disorder occurs near the center of the cell. This state of spatiotemporal disorder does not sustain itself indefinitely. Gradually, the pattern evolves toward a state that is more ordered, although the mechanism by which this occurs is hard to define.

In Fig. 4(b) the pattern is shown at $230\tau_\kappa$. Some areas of the pattern remain highly disordered, while several domains of fairly well organized waves can be seen forming on the right boundary of cell. In Fig. 4(c), recorded at $550\tau_\kappa$, the trend observed in Fig. 4(b) has continued; curved rolls have invaded most of the cell. On the right-hand side of the pattern, a billowing structure, similar to the ones in Fig. 4(a), is forming. As time proceeds, this structure expands and causes a partial relapse into disorder. In Fig. 4(d), recorded at 680 τ_κ, disorder has increased dramatically on the left-hand side of the cell, but a source on the lower right boundary has begun launching well organized straight rolls into the pattern that appear to sweep the disorder away. This effect is similar to the mechanism proposed by Aranson, Levine, and Tsimring [30] for the stabilization of chaotic spatiotemporal patterns in systems with a convective instability. In their scenario, a source emitting stable waves can eliminate spatiotemporal chaos by sweeping chaotic fluctuations to the system boundary. In our experiment, however, the source itself is not stable, as is evident from the fact that the waves in the immediate vicinity of the wall are beginning to break up. As this pattern develops, the nearly straight rolls continue to sweep across the cell, but the disorder is again partially renewed as defects appear within the straight rolls, creating more of the billowing structures seen in Fig. 4(a).

The evolution of the pattern from the disordered initial state to an ordered final state is a sequence of advances and relapses, in which progressively larger domains of traveling waves invade the pattern, sometimes breaking down into smaller domains. The configuration that ultimately results, typically after evolution at constant Rayleigh number for at least $2\times10^3\tau_\kappa$, is a pattern composed of several well defined domains of traveling waves. Invariably, this multidomain state has an overall sense of rotation in which the rolls in each of the domains are moving in the same direction around the perimeter. This is probably related to the instability of sources mentioned above, since a domain of traveling waves moving in a direction counter to its neighboring patches must result in a source and a sink of waves at the cell boundary. Although mature multidomain patterns are stable in the sense that they do not break down into the intense spatiotemporal disorder that is observed after the initiation of traveling waves or after a sudden change of Rayleigh number, these patterns do not relax toward an optimum configuration. The pattern is constantly being deformed as rolls propagate across the cell and the domain boundaries continue to move as the neighboring domains of traveling waves compete with each other.

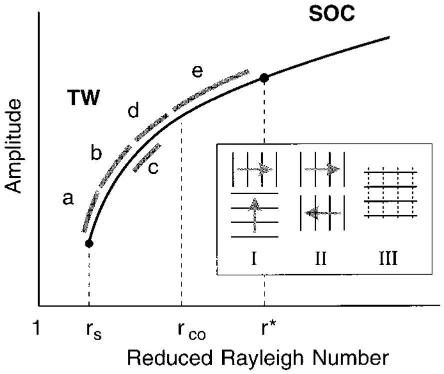

FIG. 5. Diagram of the convective amplitude as a function of Rayleigh number. The lettered regions indicate the stability of various coherent structures as indicated in the text. The inset shows the three types of defect structure discussed in the text.

B. Dependence of mature patterns on *r*

The detailed nature of a mature, multidomain state is very sensitive to the Rayleigh number. We find that the likelihood of observing a particular defect structure depends strongly on the Rayleigh number, although there is no evidence that there are well defined transitions between different TW patterns. The situation may be analogous to the transition from phase turbulence to defect turbulence in the one-dimensional complex Ginzburg-Landau equation, where the apparent transition corresponds to a rapid but continuous increase in the density of phase dislocations in the system [31].

Figure 5 is a diagram showing where the various types of patterns occur in the bifurcation diagram. The TW branch of convection is terminated at low Rayleigh number by r_s, the Rayeigh number below which straight rolls become unstable, which occurs at 1.23. In the range $1.23<r<1.25$, labeled *a* in Fig. 5, convection tends to be extinguished near domain boundaries or other defect structures, resulting in holes in the convection pattern. For $1.25\leqslant r<1.30$, labeled *b* in Fig. 5, the amplitude of the pattern is stable and the domain boundaries are most frequently the structures labeled type I in the inset of Fig. 5. The rolls on either side of the boundary are roughly perpendicular and the boundary line itself is approximately parallel to one set of rolls. The rolls parallel to the boundary always move toward the boundary (i.e., it is a sink) and the boundary moves in the same direction as these parallel rolls at a velocity somewhat slower than the roll propagation velocity. Deviations from this rectilinear configuration of up to 30° are typically observed. In this range of Rayleigh numbers, the rolls tend to be quite straight and very neatly ordered patterns are often observed, although the well defined domains sometimes break down for reasons that are not apparent. An example of a pattern observed in this regime is shown in Fig. 6(a). The pattern contains four boundaries, two type I boundaries and two poorly organized boundaries that resemble type I boundaries but contain additional defects.

If the Rayleigh number is set in the range $1.30<r<1.37$, labeled *d* in Fig. 5, the patterns have a different character. The type I domain boundaries found in region *b* still appear, but domain boundaries of type II are also

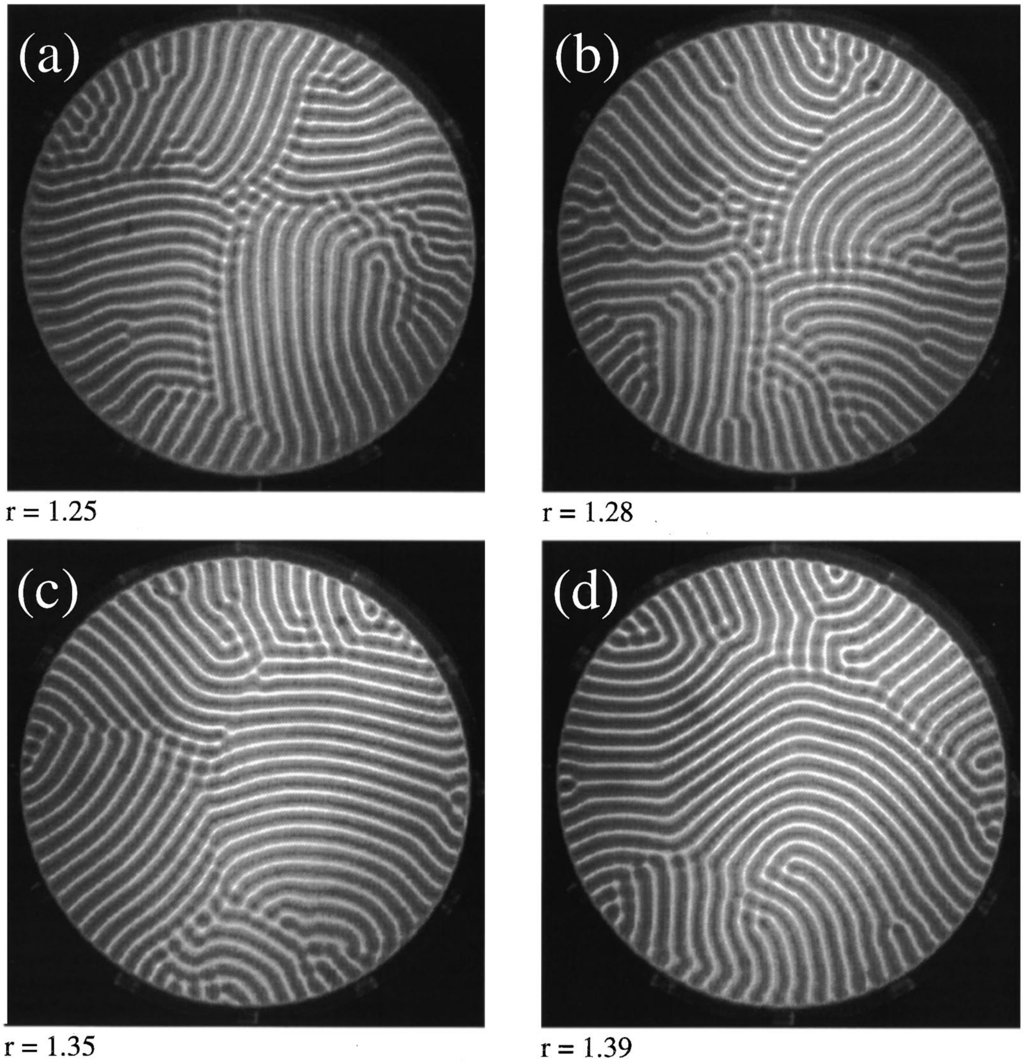

FIG. 6. Raw images of mature convection patterns for a variety of Rayleigh numbers: (a) $r=1.25$, (b) $r=1.28$, (c) $r=1.35$, and (d) $r=1.39$. The sense of rotation (see the text) is clockwise for (a) and counterclockwise for (b)–(d).

frequently observed. In the type II boundaries, which are also called ''zippers,'' [9] the rolls on either side of the boundary are approximately parallel, but propagate in opposite directions. The domain boundary is perpendicular to the rolls, or if the rolls are not perfectly parallel, the grain boundary tends to be oriented symmetrically with respect to the rolls. Although the type II boundaries sometimes appear in regimes *a* and *b*, particularly in more disordered patterns, they are more prevalent and tend to persist longer in regime *d*. At the lower Rayleigh number, the rolls on either side of a zipper glide past each other without any noticeable interaction, but as the Rayleigh number approaches the upper limit of regime *d* there seems to be an increased resistance to the shearing of rolls along the boundary line. Another difference between region *d* and region *b* is that cross-roll patches are prevalent in the former regime. The cross-roll patches, labeled as type III in the inset of Fig. 5, have been described above in connection with the disordered state. A typical pattern in region *d* is shown in Fig. 6(c). In this figure, each of the domains is moving in a counterclockwise orientation and three zippers separate the three large domains. In addition, a small cross-roll patch has formed where the three main domains come together, just to the left of the center of the cell.

If the Rayleigh number is increased further and set in the range *e*, which extends from 1.37 up to $r^{\star}$ at 1.58, type II domain boundaries are no longer observed. As the Rayleigh number is increased into this regime, the zipper states, which are typically present near the center of the cell, become pinned and an overall rotation of the pattern is observed. An example of this type of pattern is shown in Fig. 6(d). The rolls in all parts of the pattern are moving counterclockwise along the boundary. If the Rayleigh number were slightly lower, this might result in a zipper in the center of the cell, but at this Rayleigh number, the zipper becomes ''stuck'' and the entire pattern rotates. In this pattern there is visible strain where the counterpropagating rolls connect. At the high end of this range of Rayleigh number, such strain is less evident and the patterns rotate rigidly.

Above $r^{\star}$, the rigid rotation of the pattern stops and stationary overturning convection is observed. The patterns observed just above $r^{\star}$ are angular, consisting of patches of straight rolls. As we have reported elsewhere, when the Rayleigh number is increased to a high value, the pattern relaxes to a more curved texture [32]. The curved texture is characteristic of Rayleigh-Bénard convection, but the angular texture only seems to occur near $r^\star$ in the binary fluid system.

Finally, we note one additional regime, labeled c in Fig. 5, which is centered at $r=1.30$ and overlaps with regimes b and d. Regime c is a range of Rayleigh numbers in which an enhanced level of the curvature of the rolls is observed. The curvature is generally such that the divergence of the velocity vector is positive, except for small regions of negative divergence, which sometimes appear near the cell boundary. In this regime, there is also an increased tendency for orderly domain structures to break down to more disordered patterns. An example of such a pattern is shown in Fig. 6(b).

It is interesting that of all of the possible configurations of domain boundaries, only those that we have labeled type I and type II are frequently observed. Sources of straight rolls are not observed within the patterns and sinks (i.e., the head on collision of straight rolls) normally evolve into cross-roll patches, which we label as type III. Neither the type I nor type II boundaries appear to have any obvious intrinsic instabilities, although in the course of the evolution of the mature patterns they can be swept into configurations in which they are inconsistent with the circular cell boundary and disappear. The instability of zippers predicted by Aranson and Tsimring [21] was not observed, but zippers tend to be converted into type I boundaries when they interact with the cell boundary and this limits the lifetime of a zipper to about $200\tau_\kappa$ in the mature patterns. It is possible that the predicted instability would manifest itself over longer time scales.

C. The structure of ''zippers''

The type II domain boundaries, or ''zippers,'' have a fascinating structure. The rolls on either side of a zipper boundary are perpendicular to the boundary and propagate in opposite directions. The configuration is reminiscent of a shear flow, but without a Kelvin-Helmholtz instability. It should be kept in mind that the propagation of the convection rolls does not correspond to a significant mean flow in the fluid. The convection rolls are really long vortex lines, and at a zipper boundary, the vortex lines repeatedly disconnect and reconnect across the boundary as they move past each other. At low Rayleigh numbers, there is no apparent interaction between the vortex lines (the convection rolls), but as the Rayleigh number is increased, there is a resistance to the disconnection of the vortex lines, which seems to impede the movement of the rolls. At Rayleigh numbers above 1.37, the attraction of the vortex lines is sufficiently strong that they become pinned and the convection rolls are held in place, despite their natural tendency to propagate.

In Fig. 7(a), a sketch of the shadowgraph visualization of a zipper is shown. In the left panel, the zipper is aligned, and in the right panel, the rolls on either side of the domain boundary have propagated by $\lambda/4$, so that the rolls are out of phase across the zipper. The bright bars indicate descending plumes of cold fluid, the dark bars indicate ascending plumes of hot fluid, and the vortex cores are located between the dark and bright bars. In Fig. 7(b), the corresponding fluid flow is sketched for the aligned and unaligned configurations of the zipper. In the aligned state, shown in the left panel, the vortices on either side of the boundary merge together, whereas in the unaligned state, shown in the right panel, vortices of opposite sign abut, creating a region of intense shear at the boundary.

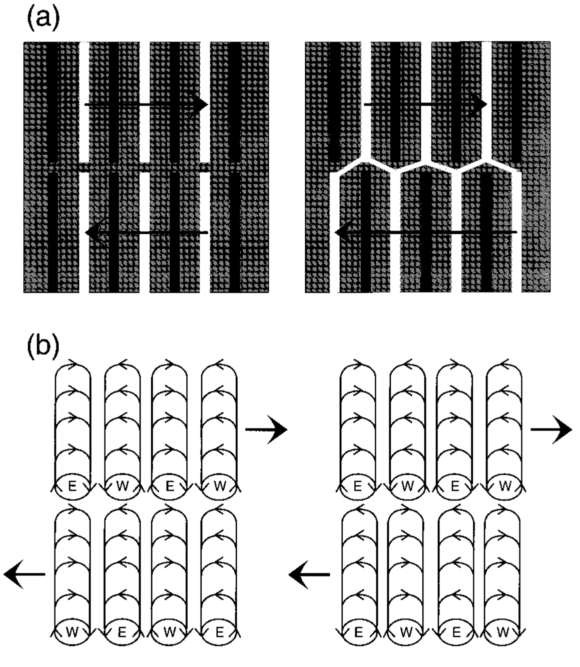

FIG. 7. (a) Representation of the shadowgraph visualization of a zipper in its aligned and unaligned configuration. (b) Sketch of the flow pattern of the zipper. W and E represent water and ethanol-rich rolls, respectively.

Even when they are aligned, the vortices on either side of the zipper are not identical. The flow patterns surrounding the vortices are clearly not the same, since the flows are time dependent, and the vortices are propagating in opposite directions. In addition, computer simulations of the TW state indicate that there is a small asymmetry in the ethanol concentration of the two rolls of a roll pair [33]. As indicated in Fig. 7(b), the right-going traveling waves consist of ethanol-rich rolls with positive vorticity and water-rich rolls with negative vorticity, whereas the left-going traveling waves have the opposite symmetry. When the rolls are aligned, vortices of the same polarity but dissimilar concentration are matched. At low Rayleigh numbers, the rolls glide past each other without interaction and the rolls apparently maintain their dissimilar concentration and detailed flow patterns, except for a very narrow region near the domain boundary. At high Rayleigh numbers, when the vortices become pinned at the domain boundary, the flow pattern and concentration difference must gradually change from the right-going to the left-going symmetry along the vortex lines. In the intermediate regime, in which the zipper continues to shear but the motion of the rolls is impeded by resistance to the disconnection and reattachment of the rolls, there must be a substantial region where the concentration and velocity fields are modified, and the transition to the pinned state presumably corresponds to the growth of this region. It is likely that it is the action of viscosity or thermal diffusion across the domain boundary that causes the modification of the fluid flow near the zipper. The other possibility, that diffusion of ethanol across the boundary modifies the concentration field, is not plausible because the time scale for mass diffusion in the liquid is too long.

V. EXTRACTION OF THE COMPLEX ORDER PARAMETER

In the analysis of stationary convection patterns, it is normally sufficient to analyze a single snapshot of the pattern to determine its state at a given moment. Fourier transform techniques can be used to measure the spectral content of the pattern [34] and heuristic algorithms can be used to measure local properties of the pattern such as the wave number or curvature [5]. In the case of traveling-wave patterns, the state of the pattern cannot be obtained from a single frame. From a practical point of view, it is necessary to determine the propagation velocity as well as the configuration of the convection rolls to specify the pattern. If the system is analyzed in terms of a model equation, then the visible pattern is interpreted as the real part of the complex order parameter and the imaginary part manifests itself only after the system has evolved for a coherence time. An algorithm is needed that can capture the kinematic properties of the traveling-wave patterns to facilitate description of the phenomena and comparison with analytical models.

For one-dimensional traveling-wave or oscillatory patterns, a very effective analysis technique known as complex demodulation may be used. The idea is to assume that the field can be written as a superposition of counterpropagating waves of the form

$$\begin{aligned} A(x,t) = {} & A_R(x,t)\cos[kx-\omega t+\phi_L(x,t)] \\ & + A_L(x,t,)\cos[kx+\omega t+\phi_R(x,t)], \end{aligned} \tag{6}$$

where A_L and A_R are slowly varying envelopes and ϕ_L and ϕ_R are phase modulations that represent local wave number variations in the pattern. By calculating the inner product of the data with the spatiotemporal carriers for left- and right-going waves and by making use of the assumption that the data have a narrow spectral content centered on the carrier frequencies, it is possible to demodulate the field and extract the amplitude and phase of the left-going and right-going components [35]. Unfortunately, this technique cannot be directly extended to two-dimensional traveling-wave patterns because a spatial carrier with a distinct wave vector cannot be found. Although the modulus of the wave vector observed in a two-dimensional pattern is restricted to a narrow range of values, the orientation of the rolls is arbitrary. Therefore the distributions of k_x and k_y are broad and the demodulation in x and y cannot be performed.

Below, we describe an algorithm that is similar to complex demodulation in that a complex amplitude is extracted from the pattern, but is flexible enough to capture the complex spatial structure of two-dimensional TW patterns. The basis of the algorithm is the fact that, despite the complex spatial structure of the TW patterns, the time series of a typical point in the pattern is periodic and has a narrow frequency spectrum. Regular oscillations are observed within domains of traveling waves and the passage of point defects or grain boundaries merely causes phase dislocations in the oscillations. The domain boundaries move slowly compared with the roll propagation velocity, so in a sequence of frames corresponding to a few oscillations of the pattern, only a small fraction of the pixels making up the image are affected by the domain boundaries and the rest execute periodic oscillations. Therefore, at a given instant of time, a mature pattern, such as those shown in Fig. 6, can be modeled as an ensemble of oscillators, one for each pixel in the image, and a description of the pattern consists of the specification of the complex amplitude and frequency of oscillation of each pixel. The complex amplitude as a function of position $A(\mathbf{x})$ is essentially the complex order parameter of the pattern. In the large domains of the mature TW patterns, the modulus of $A(\mathbf{x})$ is found to be approximately constant in time and space so the pattern's spatial structure is contained almost entirely in the phase $\phi(\mathbf{x})$ defined by

$$A(\mathbf{x}) = \|A(\mathbf{x})\| e^{i\phi(x)}. \tag{7}$$

The instantaneous time evolution of the pattern consists of the evolution of $\phi(\mathbf{x})$ and is determined by the frequency field $\omega(\mathbf{x})$ since

$$\left.\frac{\partial\phi(\mathbf{x})}{\partial t}\right|_{t=t_0} = \omega(\mathbf{x}). \tag{8}$$

In the immediate vicinity of the domain boundaries a superposition of wave components is expected and interference can cause significant modulation of $\|A(\mathbf{x})\|$. In these areas, the pattern cannot be described by the phase alone and the algorithm described below will not give complete information.

In order to calculate the amplitude and phase fields that characterize the pattern at a given instant in time, a sequence of frames corresponding to approximately 5–10 oscillation periods is selected. The sampling rate of the data is typically 10–20 samples per oscillation period, so about 100 frames are normally used. The time series a_n of each pixel in the image is multiplied by a smooth window function $e_n = \sin(n\pi/N)$, where N is the total number of points, and then Fourier transformed. The frequency of each pixel is defined as the peak value of the Fourier power spectrum. Since the time series contains only a few oscillations of the signal, the relative width of the peak in the Fourier spectrum is large, but this does not necessarily prevent the frequency from being determined with high accuracy. If we assume that the input signal is a pure sine wave, then the Fourier transform of a short section of the signal is a wide peak centered on the carrier frequency and, in principle, a Fourier transform algorithm can still be used to find the center of the peak with arbitrarily high precision. In practice, a precise determination of frequency is not meaningful if the signal to be sampled has a broad frequency spectrum and noise will limit the precision with which frequencies can be measured. The goal is to configure the Fourier transform algorithm to have sufficiently high resolution so that the accuracy of the frequency measurement is limited by the properties of the signal and not by the Fourier transform algorithm itself. The quality of the frequency determination can then be estimated from the quality of the result.

The standard fast Fourier transform (FFT) algorithm does not give adequate resolution when applied directly to the data sets. In order to get a sufficiently accurate transform, the data are first padded with zeros to 8 times its original length, which increases the density of points in the FFT spectrum by a corresponding factor. After a preliminary estimate of the frequency has been made based on the padded FFT output, a standard discrete Fourier transform is used to trace out the peak of the spectrum to whatever accuracy is desired.

Once the frequency has been found for each pixel, the complex amplitude is calculated by evaluating the inner product between the data and the Fourier component

$$A(\mathbf{x})=\frac{1}{\pi}\int_{-T/2}^{+T/2}A_{\mathbf{x}}(t)e^{i\omega t}dt=\sum_{n=0}^{N-1}a_n e_n e^{i\omega(n-N/2)}, \quad (9)$$

where $A_{\mathbf{x}}(t)$ is the windowed time series data of the pixel at location $\mathbf{x}$, defined such that $t=0$ corresponds to the midpoint of the sequence of frames. It is very important that the time origin be chosen in this way; otherwise, the phase of $A(\mathbf{x})$, which specifies the spatial pattern, will be very sensitive to noise in the determination of $\omega(\mathbf{x})$. For this choice of the time origin, the coupling of the phase to $\omega(\mathbf{x})$ is zero to first order.

Once the complex amplitude has been calculated, it is convenient to calculate the phase map $\phi(\mathbf{x})$, from which all of the properties of the pattern are subsequently derived. Manipulation of the phase presents some numerical difficulties. If the phase is stored as a real number in the domain $(-\pi,\pi)$, calculations of phase differences across the discontinuity at $\pm\pi$ require special processing, which is awkward to implement. Storing an absolute phase is not possible, since topological defects in the pattern make it impossible to assign the phase everywhere in a consistent manner. It is convenient to store the phase as a signed 16-bit integer so that the interval $(-\pi,\pi)$ maps to $(-32\,768,32\,768)$. In this case, signed integer arithmetic on the phase gives the correct phase difference in all cases.

As an illustration of this technique, 128 frames centered on the pattern shown in Fig. 6(a) were analyzed and the results are shown in Fig. 8. A frame was recorded every 15 sec, so the sequence covers 1920 sec, which corresponds to $15\tau_\kappa$, or 9 oscillation periods of the traveling-wave state. In order to prepare the data for analysis, each frame was first divided by a reference image taken with $r<r_s$ in order to compensate for nonuniformity in the shadowgraph illumination, then each frame was subject to a mild low-pass spatial filter in order to suppress broadband noise and superfluous fine scale structure in the image, such as sharp features associated with concentration gradients in the fluid layer [36]. Finally, the complex amplitude, phase, and frequency fields were calculated.

In Fig. 8(a), the phase of the complex amplitude is mapped to gray scale using a sawtooth function. A comparison with Fig. 6(a) indicates that the phase field gives a very clean representation of the pattern and resolves the ambiguity of the direction of propagation of the rolls. Figure 8(b) shows $\|A\|$, the amplitude of oscillation as a function of position. Within the large domains, $\|A\|$ is nearly constant, justifying the assumption that the pattern is determined mainly by the phase. As expected, some modulation of $\|A\|$ is observed at the domain boundaries where the wave fields overlap. The frequency $\omega(\mathbf{x})$ is shown in Fig. 8(c). It is interesting that the frequency varies widely over the pattern. The frequency near the domain boundaries at the center of the cell is more than a factor of 2 smaller than it is near the cell boundary. Clearly, the domain boundaries have a profound influence on the TW state, despite the fact that most of the pattern consists of straight rolls.

The remaining three panels in Fig. 8 show quantities that are derived from $\phi(\mathbf{x})$. Since the pattern consists mainly of waves, it is convenient to rewrite the phase in the form

$$\phi(\mathbf{x})=\mathbf{k}(\mathbf{x})\cdot\mathbf{x}. \quad (10)$$

Here $\mathbf{k}(\mathbf{x})$ is the local wave vector, which is easily extracted from the phase map using

$$\mathbf{k}(\mathbf{x})=\boldsymbol{\nabla}\phi(\mathbf{x}). \quad (11)$$

Writing $\mathbf{k}=\hat{\mathbf{n}}k$, we can evaluate the modulus of the wave vector k and the unit vector $\hat{\mathbf{n}}$, which is normal to the rolls and points in the direction of propagation. A map of the wave number k is shown in Fig. 8(d). The gray scale is chosen to have high contrast in order to make the small variations in wave number visible. The algorithm gives accurate measurement of the wave number with very high spatial resolution, even in fairly close proximity to grain boundaries and defects. The stripes that are visible in the wave number maps at the domain boundaries themselves indicate areas where significant overlap of waves occurs. Point singularities in the wave number that are expected near dislocations in the pattern are transformed into short line singularities, corresponding to the trajectories of the defects during the sequence of frames. Nevertheless, the calculated wave number is accurate in the neighborhood of the defect, except for the immediate vicinity of the singularity, where the wave number is not well defined. As expected, the wave number, normalized to the cell height, is narrowly peaked at π. There are some broad areas of slightly compressed or dilated rolls, but the variation of the wave vector over the pattern is much smaller than the variation observed in the frequency. The angle between $\hat{\mathbf{n}}$ and the horizontal axis is shown in Fig. 8(e).

Also of interest is the curvature, shown in Fig. 8(f), which is calculated using the expression

$$c(\mathbf{x})=\boldsymbol{\nabla}\cdot\hat{\mathbf{n}}. \quad (12)$$

The curvature is a second derivative of the phase field and so the high-frequency noise that is visible in the wave number field is further amplified. In order to reduce this noise, the divergence in Eq. (12) is calculated over a span of 8 pixels rather than from adjacent pixels. This has the effect of suppressing the high-frequency noise while maintaining a resolution of about one cell height. Since $\hat{\mathbf{n}}$ points in the direction of propagation, Eq. (12) assigns a positive curvature to rolls that diverge and negative curvature to rolls that converge, resolving the ambiguity that is present in stationary patterns. The data of Fig. 8(f) indicate a pervasive weak positive curvature, with small regions of strong positive curvature near domain boundaries and some small areas of negative curvature near the cell boundary.

The same analysis was also applied to the pattern presented above in Fig. 6(c) and the results are shown in Fig. 9. This pattern was recorded at $r=1.35$ and is organized around

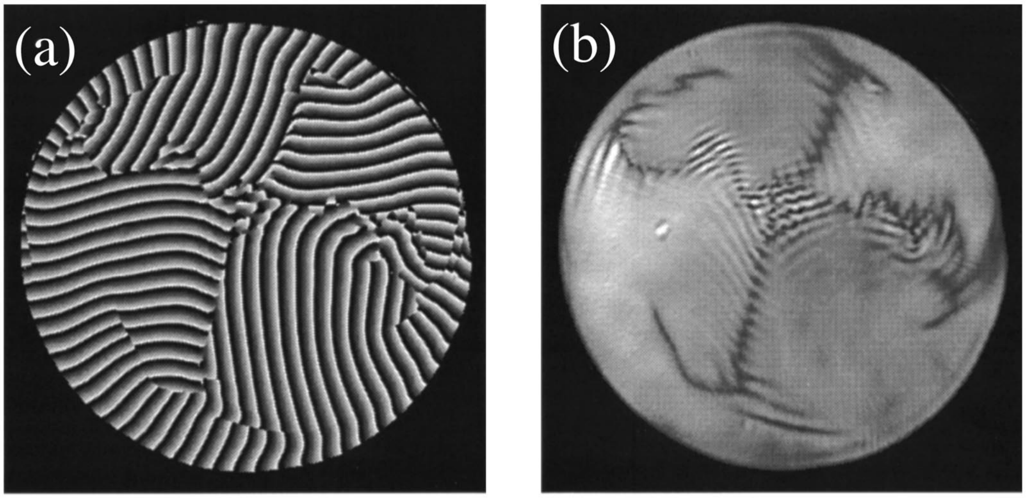

Phase

Modulus (0,0.27)

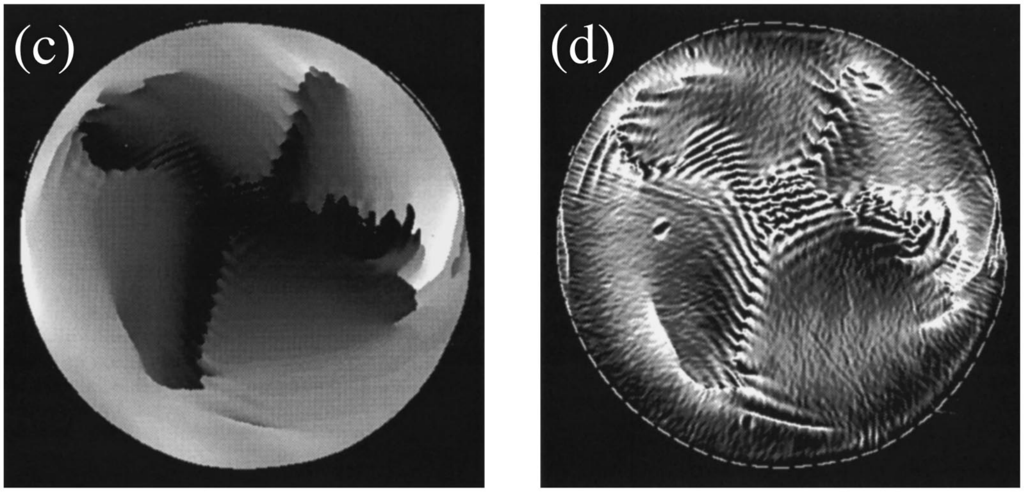

Frequency (0.26,0.58)

Wave number (2.75,3.5)

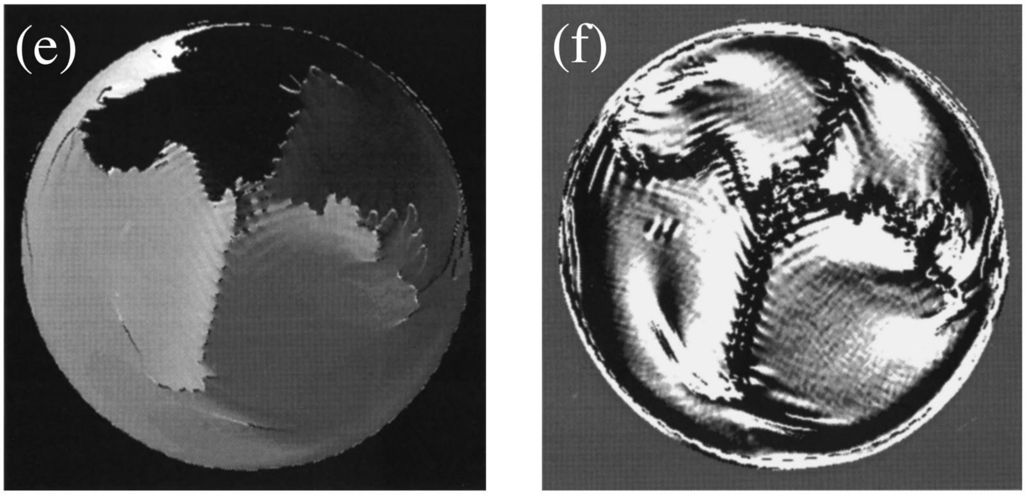

Direction

Curvature (-0.05,+0.05)

FIG. 8. Analysis of the pattern shown in Fig. 6(a), recorded at $r=1.25$: (a) phase, (b) modulus $\|A\|$, (c) frequency $\omega(\mathbf{x})$, (d) wave number $\|k\|$, (e) direction $\tan^{-1}(k_y/k_x)$, and (f) curvature $\boldsymbol{\nabla}\cdot\hat{\mathbf{n}}$. Where applicable, numerical limits for the gray scales are shown below the images. The small spot to the left of center in panel (d) results from an optical defect in the visualization system.

three type II (zipper) boundaries, which are often seen at this value of r. The six panels of Fig. 9 correspond to those of Fig. 8, although it has been necessary to change some of the scales in order to accommodate the data. The variation of the frequency is qualitatively the same, with smaller values near the domain walls, although the overall frequency is lower at this value of r and the relative variation is not quite as large as in Fig. 8. The conclusion is that oscillation frequency is

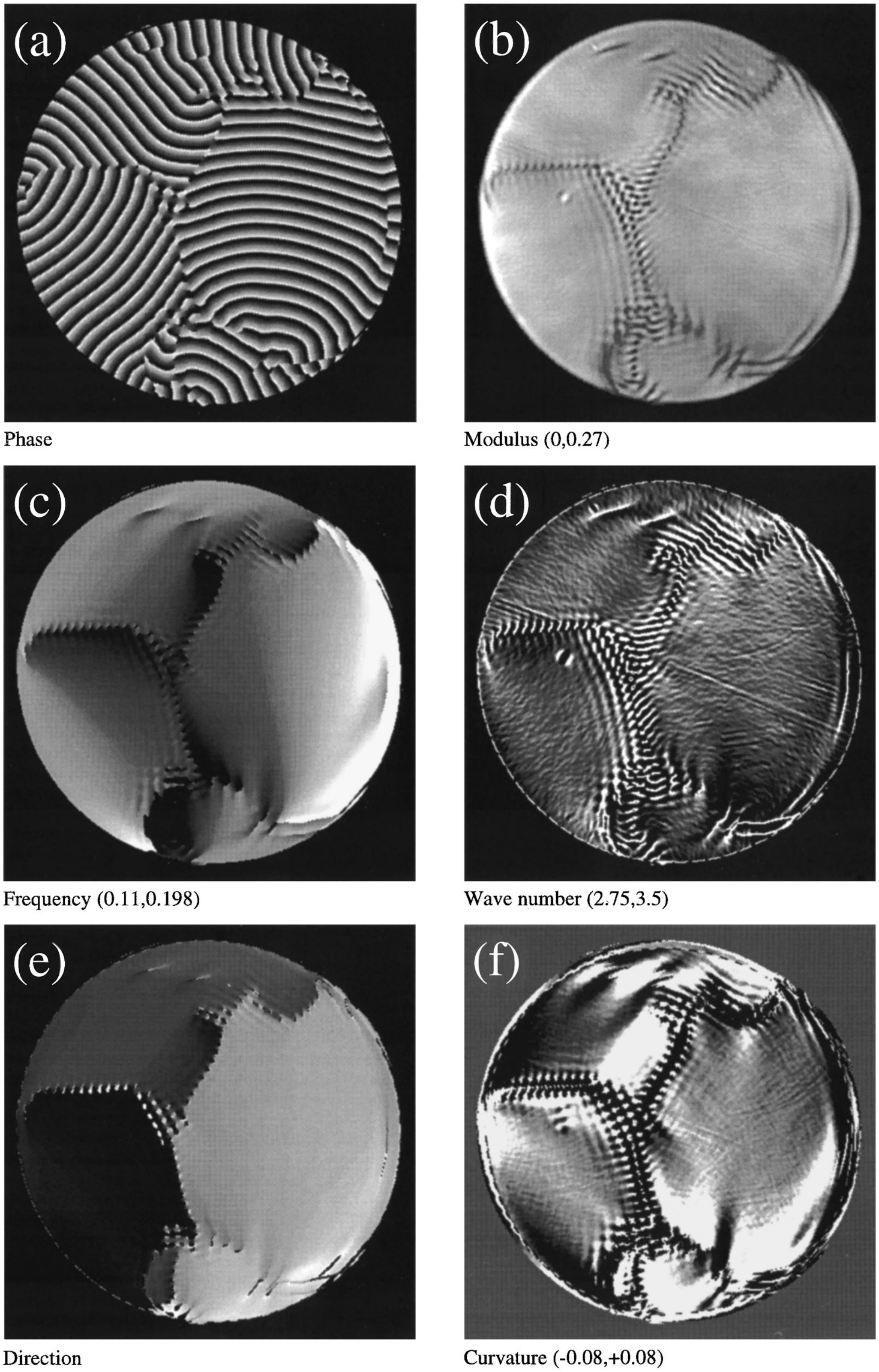

FIG. 9. Analysis of the pattern shown in Fig. 6(c), recorded at $r=1.35$: (a) phase, (b) modulus, (c) frequency, (d) wave number, (e) direction, and (f) curvature. Where applicable, numerical limits for the gray scales are shown below the images.

reduced near the zippers, even though for this value of r, the zippers appear to move freely. The direction map clearly differentiates the zipper boundaries and the curvature plot also exhibits a pervasive positive curvature with regions of intense curvature that are somewhat more prominent at $r=1.35$ than at $r=1.25$.

Finally, in Fig. 10 an analysis of the more disordered pattern presented above in Fig. 4(c) is shown. This pattern

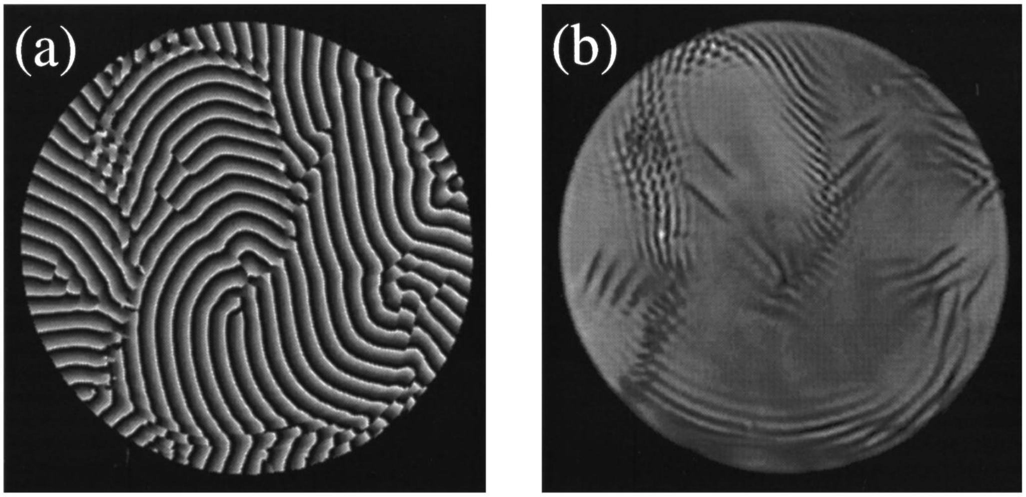

Phase

Modulus (0,0.25)

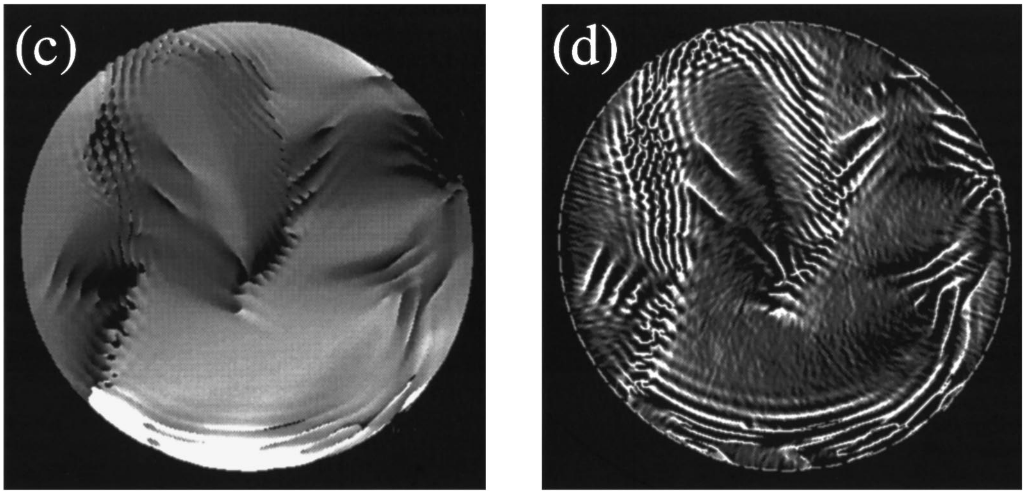

Frequency (0.16,0.27)

Wave number (2.75,3.5)

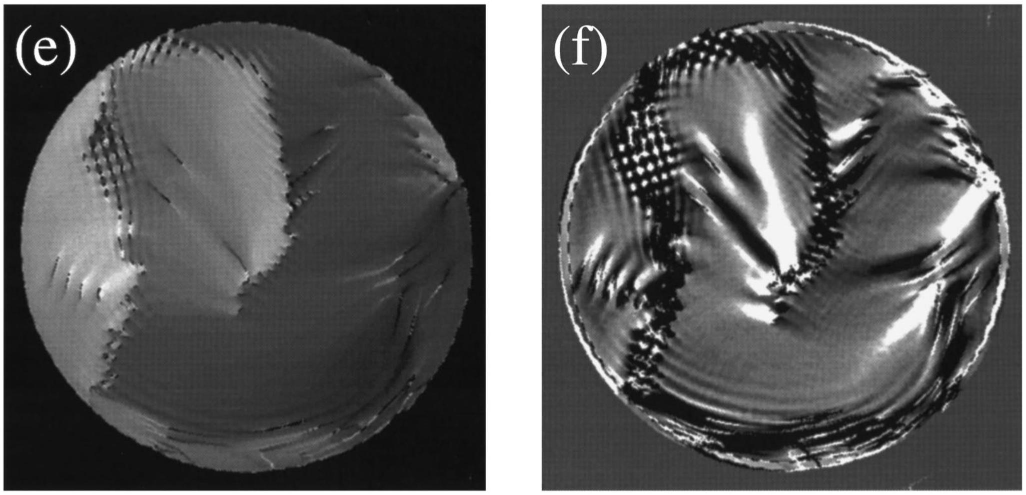

Direction

Curvature (-0.25,+0.25)

FIG. 10. Analysis of the pattern shown in Fig. 4(c), recorded at $r=1.28$ during the initial development of a pattern: (a) phase, (b) modulus, (c) frequency, (d) wave number, (e) direction, and (f) curvature. Where applicable, numerical limits for the gray scales are shown below the images.

represents a state that is intermediate between the intense disorder of the initiation of TW convection and the domains of nearly straight rolls in the mature patterns. The pattern has not yet reached a state of uniform rotation and not all domains are in contact with the cell boundary. The frequency has a fairly large spread with high values where rolls move along the boundary and low values near sources of rolls, whether they are at the interior of the pattern or at the bound-

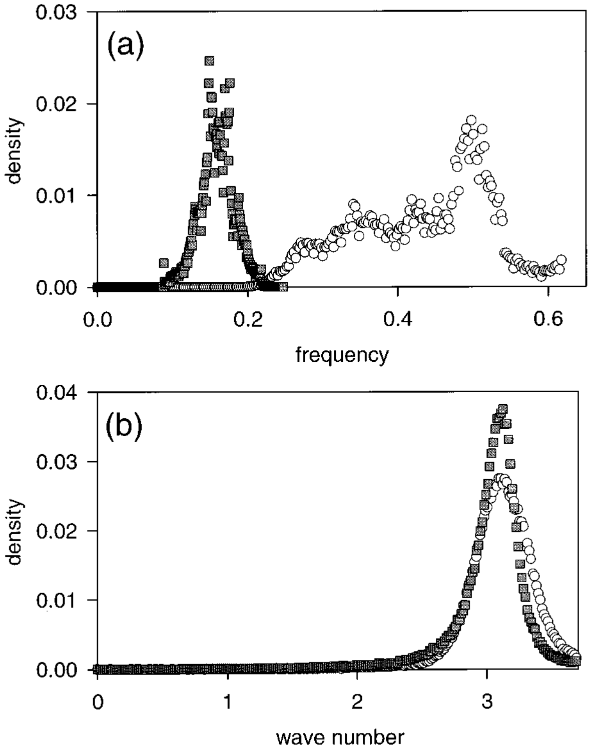

FIG. 11. Distribution functions for (a) the frequency and (b) the wave number. The unit of distance is the cell height and the unit of time is the vertical thermal diffusion time $\tau_\kappa = 124$ sec. White circles are data at $r = 1.25$ from Fig. 8 and gray squares are data at $r = 1.35$ from Fig. 9.

ary. As in the mature patterns, the wave number does not vary widely. As expected, more overlap of waves is observed in this pattern than in the more ordered patterns.

In Fig. 11, the distributions of frequency and wave number are shown for the mature patterns at $r = 1.25$ and $r = 1.35$. In both cases, the spread of frequencies is substantial, while the wave number is sharply peaked. This is in sharp contrast to the results for one-dimensional patterns, where the frequency and wave number both vary widely and maintain a well-defined dispersion relation [18]. In Fig. 12, the joint distributions of wave number and frequency are shown for the data at $r = 1.25$ and $r = 1.35$. In both cases, the correlation between frequency and wave number is weak and bears no resemblance to the dispersion curves that are observed in the one-dimensional system. Consideration of the frequency maps of Figs. 8(c) and 9(c) and of the distribution functions in Fig. 12 indicates that the TW frequency at a given point in the two-dimensional patterns is strongly correlated with defect structures in the immediate neighborhood, but not strongly correlated with the local wave number.

VI. DEFORMATION OF TRAVELING-WAVE PATTERNS

In the preceding section, we discussed how it is possible to obtain a complex amplitude field that describes the state of a traveling-wave pattern. Each point in the field is represented as an oscillator with a specified complex amplitude and frequency. The spatial pattern, including information about the direction of propagation of waves, is determined by the relative phases of the oscillators and the evolution of the pattern in time corresponds to the rotation of the complex amplitudes at well defined frequencies. By examining the relationship between the phase and frequency fields, it is possible to characterize the rate of deformation of the pattern at a given instant.

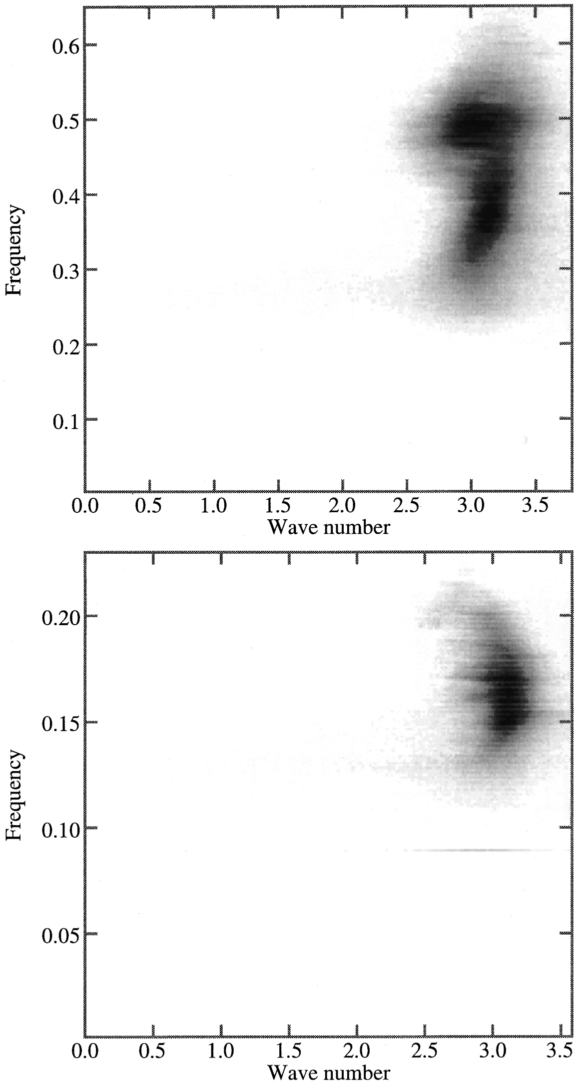

FIG. 12. Distribution of wave number and frequency for (a) a mature pattern recorded at $r = 1.25$ and (b) a mature pattern recorded at $r = 1.35$.

It is clear that a region of the pattern can only evolve without deformation if the frequency of oscillation is the same throughout the region. If the oscillation frequency is different at two points in the pattern, then a different number of rolls will pass these points in a given time interval and the pattern will be deformed. The nature of the local deformation depends on the relationship between the gradient of the frequency field $\nabla\omega$ and the direction of propagation $\hat{\mathbf{n}}$. If $\hat{\mathbf{n}}$ and $\nabla\omega$ are parallel in a region of the pattern, then the frequency is higher for rolls leaving the region than for rolls entering the region and the pattern will be subject to a local stretching. If $\hat{\mathbf{n}}$ and $\nabla\omega$ are antiparallel, then the opposite is true and the pattern will be locally compressed. Similarly, if $\hat{\mathbf{n}}$ is

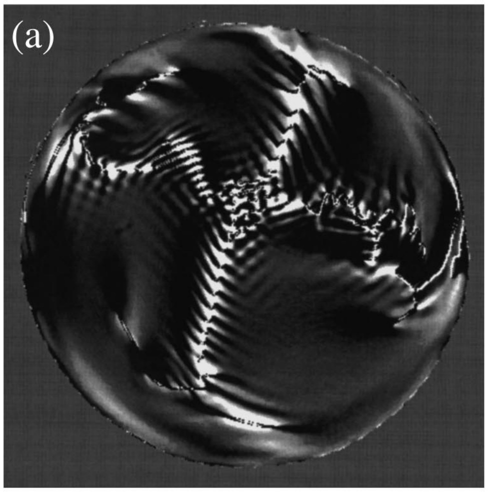

Twist (-0.0065,+0.0065)

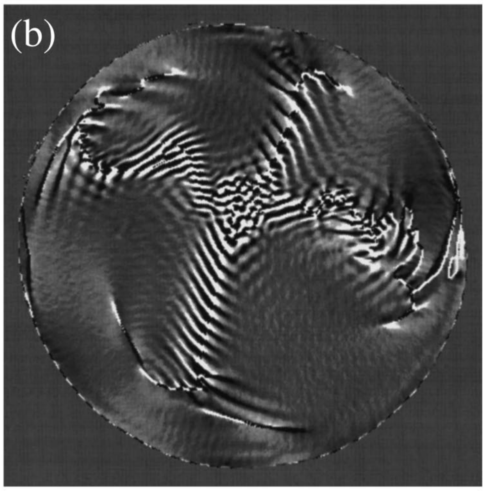

Stretch (-0.0065,+0.0065)

FIG. 13. Deformation of the pattern at $r = 1.25$: (a) twist $\frac{1}{2}\pi k \boldsymbol{\nabla}\omega \times \hat{\mathbf{n}}$ and (b) stretch $\frac{1}{2}\pi k \boldsymbol{\nabla}\omega \cdot \hat{\mathbf{n}}$. Distance is in units of cell height and time is in units of $\tau_\kappa = 124$ sec.

perpendicular to $\boldsymbol{\nabla}\omega$, then more rolls will pass on one side of the region than on the other and the pattern will twist locally.

The stretching of the pattern can be determined by evaluating the stretch function

$$S(\mathbf{x}) = \frac{1}{2\pi k} \boldsymbol{\nabla}\omega \cdot \hat{\mathbf{n}}, \tag{13}$$

where a positive value indicates stretching and a negative value indicates compression. Similarly, the twisting of the pattern is specified by the twist function

$$T(\mathbf{x}) = \frac{1}{2\pi k} \boldsymbol{\nabla}\omega \times \hat{\mathbf{n}}, \tag{14}$$

where a positive value indicates counterclockwise rotation and a negative value indicates clockwise rotation. Another straightforward way to combine frequency and phase information is to evaluate the phase velocity, which is defined by $v = \omega/k$.

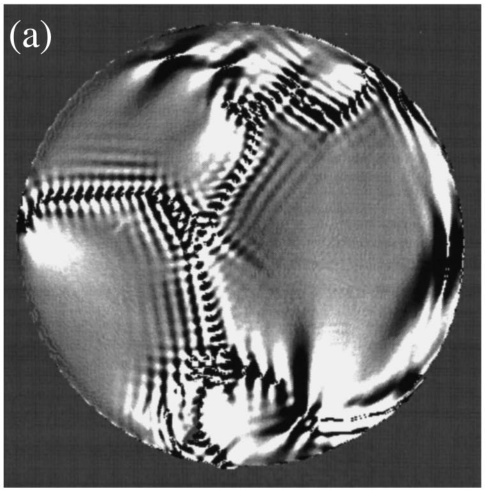

Twist (-0.0019,+0.0019)

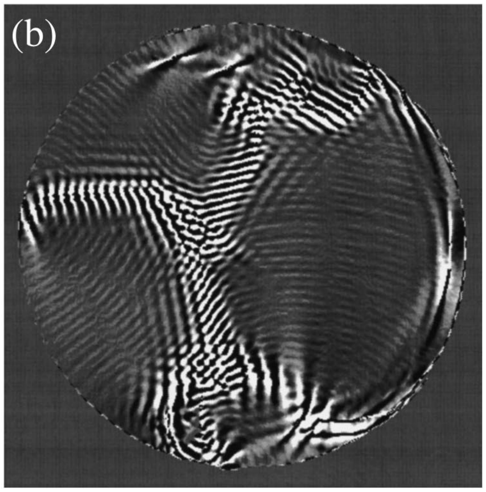

Stretch (-0.0019,+0.0019)

FIG. 14. Deformation of the pattern at $r = 1.35$: (a) twist $\frac{1}{2}\pi k \boldsymbol{\nabla}\omega \times \hat{\mathbf{n}}$ and (b) stretch $\frac{1}{2}\pi k \boldsymbol{\nabla}\omega \cdot \hat{\mathbf{n}}$. Distance is in units of cell height and time is in units of $\tau_\kappa = 124$ sec.

In Fig. 13, the twist and stretch functions are shown for the data at $r = 1.25$. The gray scale is defined so that black corresponds to a negative value of the variable, white corresponds to a positive value, and neutral gray (the field background) corresponds to zero. The units of stretch and twist are the same and the gray scales are scaled identically in the stretch and twist plots. Figure 13(a) indicates a dominant clockwise twist of the convection rolls in the pattern. The clockwise twist of the rolls corresponds with the clockwise global rotation of the pattern and is a manifestation of the fact that the propagation velocity is larger at the cell boundary than it is near the center of the pattern. The stretch function, in contrast, appears to be indistinguishable from zero over the entire pattern except for the domain boundaries themselves, which the algorithm identifies as areas of violent deformation. The absence of significant stretching or compression is consistent with the narrow wave number distribution of the pattern. In Fig. 14, the twist and stretch functions are shown for the corresponding data at $r = 1.35$. The general properties are the same. Counterclockwise twisting of the pattern is prominent and consistent with the counterclockwise global rotation of the pattern. Stretching is negligible

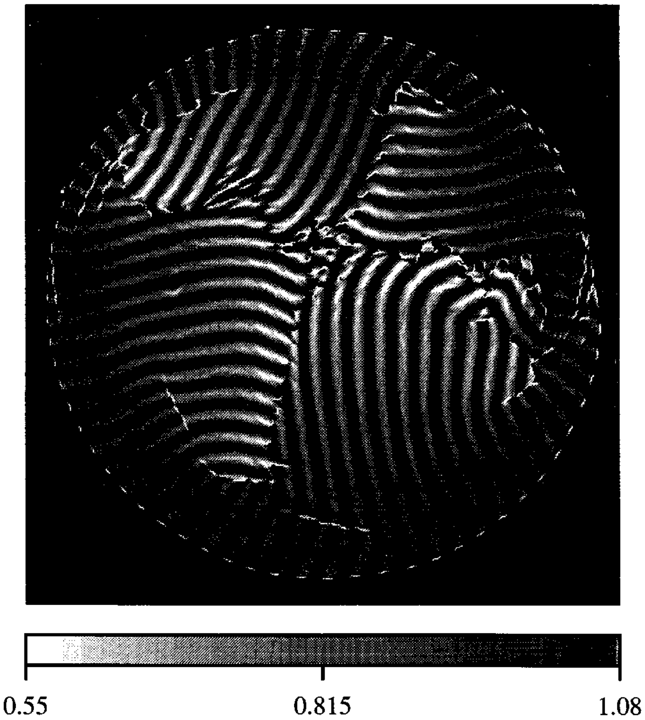

FIG. 15. Color plot of velocity at $r=1.25$ in units of h/τ_κ, where h is the cell height. The velocity is encoded as the hue of the pattern.

except for a few narrow areas associated with defects or domain walls.

Finally, the roll velocity is represented in Figs. 15 and 16. In these plots, the brightness of the field indicates the pattern and the shading indicates the velocity. Yellow rolls are moving slowly and blue rolls are moving rapidly, with gray corresponding to an intermediate value. In this plot, the slow propagation speed in the vicinity of both type I and type II domain boundaries is evident.

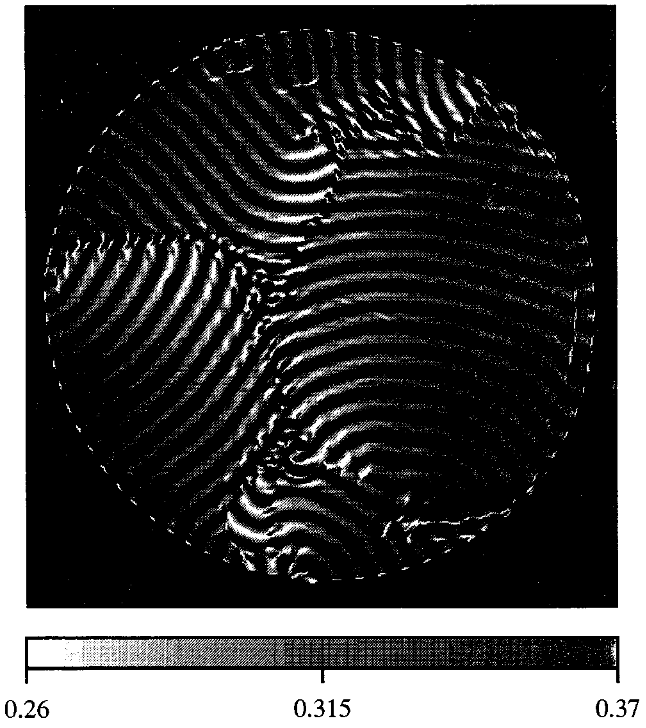

FIG. 16. Color plot of velocity at $r=1.35$ in units of h/τ_κ, where h is the cell height. The velocity is encoded as the hue of the pattern.

VII. DISCUSSION

A. Traveling-wave analysis algorithm and comparison with analytical models

If we compare a traveling-wave pattern with the pattern observed one coherence time later, every pixel in the pattern will have changed, although the significant coherent structures, the domain walls and local deformations of the waves, will have changed very little. An important goal in analyzing traveling-wave patterns is to separate the evolution of the structure of the pattern from the simple propagation of waves. The algorithm described above is intended to fulfill this goal. It takes advantage of the incessant oscillation of the pattern to generate separate representations of the phase and amplitude of the traveling waves and the frequency field gives a measurement of the ‘‘velocity’’ of the pattern, making it possible to characterize the instantaneous rate of deformation. This algorithm also has the advantage of being able to measure the direction of propagation and wave number in close proximity to defect structures, which is useful in studying the domain walls that appear to control the evolution of the pattern.

The most obvious use of this technique is to measure the kinematic properties of a TW pattern, but we anticipate that it will also be useful in making comparisons with model equations. In pure fluids, the patterns relax toward an optimum configuration and the criterion for a successful model is that it is able to replicate the stable configuration, including its basin of attraction and secondary instabilities. Strictly speaking, in TW patterns, there is no stable configuration and an effective means of comparison would instead be to use an observed configuration as an initial configuration for the model equation and see if the model reproduces the kinematic properties of the system such as the frequency field.

Although the algorithm is very successful in analyzing the mature patterns, it has some limitations. It is much less useful in studying the disordered patterns where there is a high density of defects. Also, the analysis techniques for extracting wave number and other properties depend on the assumption that the pattern consists of a single wave with phase deformations and therefore it is not able to describe the counterpropagating waves observed in small amplitude states or near domain boundaries.

There are some obvious extensions of this algorithm, which are planned to be the subject of future work. One possibility is to perform a complex demodulation of each pixel in order to evaluate the deformation of the phase field as a function of time. Another is to simply let the pattern propagate forward in time by letting each complex amplitude continue to rotate at the measured frequency. This can be compared with the actual evolution of the pattern to determine the ‘‘acceleration’’ of the pattern. Finally, the superposition of waves near domain boundaries may be studied by performing a full three-dimensional complex demodulation of the wave field in the vicinity of a domain wall.

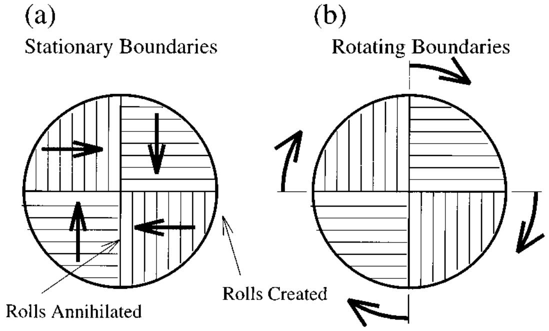

FIG. 17. Schematic representation of the hypothetical movement of domains in a TW convection pattern. In (a) the domains are stationary and the twist function is zero and in (b) the pattern rotates rigidly and the twist function corresponds to the rate at which rolls attached to the boundary are observed to orbit the cell.

B. Quenching of disorder and the transition to a rotating TW pattern

When traveling-wave convection is initiated, especially if the transition to the TW state occurs via a rapid change of the Rayleigh number, a highly disordered state is first created that consists of defect structures and areas of traveling waves that are only a few wavelengths in extent. At this stage the central area of the TW pattern seems to evolve without strong interaction with the system boundary. During the subsequent evolution of the pattern, there is an overall trend toward an increase in the domain sizes until the average domain size is of the order of the convection cell and the cell boundaries become a strong influence on the pattern. Typically, there is an intermediate stage of the evolution of the pattern in which well defined domains are observed that are not in contact with the cell boundary, such as the pattern shown in Figs. 4(c) and 10.

The increase in domain size seems to be associated with three separate mechanisms. There is a tendency for the small domains embedded in the pattern to become more organized over time, creating larger domains; sources at the system boundary begin emitting waves that tend to sweep the disorder away, as in Fig. 4(d), and waves propagating along the system boundary can grow, encroaching on the disordered patterns, as in Fig. 4(b). The progression is not steady, or monotonic, as ordered structures frequently become destabilized and break down before a mature multidomain pattern finally forms.

An interesting question is whether the decrease in the disorder and the associated increase in the average domain size in the traveling-wave system is analogous to the domain coarsening that has been studied experimentally and theoretically in rotating Rayleigh-Bénard convection [37,38]. In the rotating system, in which there are no traveling waves, the growth of domains seems to be an intrinsic property of the pattern dynamics, whereas in binary fluid convection the boundary apparently plays an important role in the trend toward larger domains. A more appropriate context for understanding the behavior of the TW patterns may be the scenario described by Aranson, Levine, and Tsimring, in which a source can emit stable waves that sweep chaotic fluctuations to the system boundary [30]. This mechanism works even if the waves are unstable, as long as it is a convective instability so that chaotic fluctuations cannot backpropagate to the source point. Preliminary observations suggest that the increase in order observed in our experiment proceeds along these lines, although the situation is complicated by the fact that the sources are not stable over long periods of time.

It is also striking that the mature patterns always have a well defined sense of rotation, with rolls attached to the circular cell boundary moving in the same direction. The direction of rotation varies from run to run, but once established, never reverses itself during a run. Oddly enough, if we were only to look at the rolls attached to the cell boundary, we would see them orbit the cell much as they do in one-dimensional experiments performed in an annular convection cell, and there appears to be a strong analogy between these systems [39]. The structure of the center of the pattern can be interpreted as reflecting the need for the pattern to satisfy several inconsistent conditions. These conditions are that the roll orientation at the edge of the pattern is perpendicular to the boundary, that the rolls remain straight with a wavelength equal to twice the cell height, and that the rolls maintain a uniform propagation velocity. At low Rayleigh number, shearing of the rolls at domain boundaries in the center of the pattern makes it possible for all three conditions to be approximately fulfilled, and as we have shown above in Sec. IV, the detailed configuration of these domain boundaries depends sensitively on the Rayleigh number. At higher Rayleigh numbers, near $r^{\star}$ on the TW branch, the rolls become pinned at the internal domain boundaries and the condition of uniform propagation velocity is violated as the pattern rotates rigidly. At the edge of the pattern adjacent to the system boundaries traveling-wave convection is maintained, but the propagation velocity at the center of the pattern goes to zero.

The rotation of the TW patterns is obviously related to the twist function [Eq. (14)], which is plotted above in Figs. 13(a) and 14(a). As expected, the direction of twisting of the mature patterns at $r=1.25$ and $r=1.35$ corresponds with the sense of rotation of the pattern. It is informative to make a quantitative comparison of the rate of twisting with the rate at which rolls orbit the cell at the system boundary for data at $r=1.25$. As can be determined from Fig. 15, the rolls at the boundary propagate at a velocity of $1.2d/\tau_K$ and therefore require about $140\tau_K$, or 5 h, to complete one orbit of the convection cell. In the large domains the mean value of the twist function, shown in Fig. 13(a), is $T=0.0035\tau_K^{-1}$. The amount of time required for twisting rolls to undergo one rotation is $1/T$, and this implies that about $285\tau_K$, or 10 h, is required for a domain of rolls to complete one rotation. The twisting rate is therefore only half that which would be observed in a rigidly rotating pattern. The twisting rate also corresponds with the observed rate of precession of the internal domain boundaries, since the domain boundaries maintain a fixed orientation with respect to the roll convection rolls.

Using the basic pattern observed in Fig. 8 as a guide, it is useful to consider two limiting cases of how the pattern can rotate in the presence of domain boundaries. One limit is that the domain boundaries remain stationary, with rolls in each domain being created at a source near the cell boundary and being annihilated at the internal domain boundary, as shown in Fig. 17(a). In this case, the twist function for the pattern is zero and the propagation velocity is uniform. In the other limit, the entire pattern rotates and the domain boundaries are advected with the convection rolls as they orbit the cell, as shown in Fig. 17(b). In this case no rolls are created or annihilated; the rate of twisting is simply equal to the rate at which rolls at the boundary orbit the cell and the roll velocity is proportional to the distance from the center of the pattern. Crudely speaking, the fact that the rolls within the domains are twisting half as fast as the rate at which rolls orbit the cell indicates that the observed evolution of the pattern is halfway between a rigidly rotating pattern of Fig. 17(b) and the stationary array of domains of Fig. 17(a). Viewed from a reference frame that rotates at the roll twisting rate, the pattern would appear like Fig. 17(a), with zero twist and stationary domain boundaries. In this rotating frame, the rolls propagate at a uniform velocity equal to the velocity observed at the center of the cell in the laboratory frame.

C. Failure of dispersion relations

It is very interesting that the TW patterns, especially at $r=1.25$, have a very broad distribution of frequency but a narrow distribution of wave number (see Fig. 11). In previous work on one-dimensional TW states, wave number and frequency both varied substantially but maintained a well defined dispersion relation, which does not seem to be consistent with the data shown in Fig. 12. The narrow wave number distribution is probably related to the fact that rolls are created and annihilated freely at the domain boundaries and the wave number remains within the Eckhaus stable band. The broad distribution of frequency is suprising under these circumstances.

The results presented above seem to indicate that the frequency is strongly correlated with the presence of defects in some finite neighborhood. Presumably the frequency is also related to the wave number, but this relationship does not manifest itself because the wave number is narrowly distributed. It is doubtful that such a complicated dependence of the frequency on the pattern could be obtained from a simple model, such as the Swift-Hohenberg equation, which depends only on the local properties of the patterns and obeys a strict dispersion relation. Probably the inclusion of nonlocal terms or an additional field would be necessary to reproduce the behavior of the physical system.

A possible physical explanation for the anomalous frequency distribution is that the disordered flow patterns that are present in the defects upset the ethanol concentration field in the vicinity of the defect. It is known that mean flows are associated with defect structures in stationary convection [40] and similar effects in the mixture could pump ethanol into or out of various regions of the pattern or upset the delicate concentration gradients in nearby convection rolls. If this were the case, the effective separation ratio would not be constant, but would vary in time and space as the defect structures evolve. The properties of the traveling-wave state are very sensitive to the ethanol concentration gradients and it is not hard to imagine that the traveling-wave velocity could be significantly affected in such a situation.

VIII. CONCLUSION

One primary result of this paper is a survey of the properties of two-dimensional traveling-wave convection patterns in a large aspect ratio cylindrical container. We have described the transition from a disordered initial state to a well organized pattern consisting of several domains of traveling waves and we have discussed the dynamics of the domain boundaries, which are the primary features of the mature patterns. We have found that the prevalence of these boundaries and the general character of the TW patterns is quite sensitive to Rayleigh number. The second important result is an algorithm that allows the extraction of the complex order parameter and frequency field from experimental convection patterns. The complex amplitude describes the instantaneous configuration, including information about the direction of propagation of waves, and the frequency field gives the instantaneous rate of propagation and deformation in the pattern. We have used this algorithm to investigate the basic kinematic properties of the mature TW patterns.

It is found that the patterns have a very broad distribution of frequency, but a narrow distribution of wave number, which seems to be at odds with previous work on one-dimensional patterns and with the standard model equations. Some of the properties observed in our system, such as the global rotation of patterns, are clearly related to the cylindrical geometry of the cell, while others, such as the transition from disordered to ordered patterns, are probably independent of the geometry. Future goals of this work are a detailed comparison of the evolution of TW patterns with analytical models and investigation of patterns in other geometries and at higher aspect ratio.

ACKNOWLEDGMENTS

We would like to acknowledge stimulating discussions with Lev Tsimring, Boris Malomed, Patrick Diamond, and Igor Aranson. We would also like to acknowledge the involvement of Keith D. Eaton in a preliminary survey of patterns in this experiment. This work was supported by the U.S. Department of Energy under Grant No. DE-FG03-90ER14148.

---

[1] M. C. Cross and P. C. Hohenberg, Rev. Mod. Phys. **65**, 851 (1993).
[2] M. S. Heutmaker, P. N. Fraenkel, and J. P. Gollub, Phys. Rev. Lett. **54**, 1369 (1985).
[3] M. C. Cross, Phys. Rev. A **25**, 1065 (1982).
[4] G. Ahlers, D. S. Cannell, and V. Steinberg, Phys. Rev. Lett. **54**, 1373 (1985).
[5] M. S. Heutmaker and J. P. Gollub, Phys. Rev. A **35**, 242 (1987).
[6] S. W. Morris, E. Bodenshatz, D. S. Cannell, and G. Ahlers, Phys. Rev. Lett. **71**, 2026 (1993).
[7] Y. Hu, R. E. Ecke, and G. Ahlers, Phys. Rev. Lett. **74**, 391 (1995).
[8] M. C. Cross and Y. Tu, Phys. Rev. Lett. **75**, 834 (1995).

[9] R. W. Walden, P. Kolodner, A. Passner, and C. M. Surko, Phys. Rev. Lett. **55**, 496 (1985).

[10] P. Kolodner, Phys. Rev. E **47**, 1038 (1993).

[11] K. Lerman, D. A. Cannell, and G. Ahlers, Phys. Rev. E **53**, R2041 (1996). This paper describes growth and collapse of small-amplitude waves in a 1% ethanol mixture. We have observed the same phenomena in our large-aspect-ratio convection cell.

[12] P. Kolodner, J. A. Glazier, and H. Williams, Phys. Rev. Lett. **65**, 1579 (1990).

[13] E. Kaplan, E. Kuznetsov, and V. Steinberg, Phys. Rev. E **50**, 3712 (1994).

[14] K. Lerman, E. Bodenschatz, D. S. Cannel, and G. Ahlers, Phys. Rev. Lett. **70**, 3572 (1993).

[15] P. Kolodner, Phys. Rev. Lett. **66**, 1165 (1991).

[16] V. Steinberg, W. Moses, and J. Fineberg, Nucl. Phys. B **2**, 109 (1987).

[17] W. Barten, M. Lücke, and M. Kamps, in *Nonlinear Evolution of Spatio-Temporal Structures in Dissipative Continuous Systems*, edited by F. H. Busse and L. Kramer (Plenum, New York, 1990), pp. 131–148.

[18] G. W. Baxter, K. D. Eaton, and C. M. Surko, Phys. Rev. A **46**, R1735 (1992).

[19] J. J. Niemela, G. Ahlers, and D. S. Cannell, Phys. Rev. Lett. **64**, 1365 (1990).

[20] M. Bestehorn, R. Friedrich, and H. Haken, Z. Phys. B **75**, 265 (1989).

[21] I. Aranson and L. Tsimring, Phys. Rev. Lett. **75**, 3273 (1995).

[22] P. Manneville, *Dissipative Structure and Weak Turbulence* (Academic, Boston, 1990).

[23] A. A. Predtechensky *et al.*, Phys. Fluids **6**, 3923 (1994).

[24] L. D. Landau and E. M. Lifshitz, *Fluid Mechanics*, 2nd ed. (Pergamon, Oxford, 1987), Vol. 6.

[25] P. Kolodner, H. Williams, and C. Moe, J. Chem. Phys. **88**, 6512 (1988).

[26] A clear and concise summary of the theory and phenomenology of binary fluid convection is given by Cross and Hohenberg in their review of nonequilibrium pattern formation [1]. A treatment with greater emphasis on the physical mechanisms is found in Mannville's text [22].

[27] D. R. Ohlsen, S. Y. Yamamoto, C. M. Surko, and P. Kolodner, Phys. Rev. Lett. **65**, 1431 (1990).

[28] P. Kolodner, Phys. Rev. A **44**, 6448 (1991).

[29] A. La Porta (unpublished).

[30] I. Aranson, H. Levine, and L. Tsimring, Phys. Rev. Lett. **72**, 2561 (1994).

[31] D. A. Egolf and H. S. Greenside, Phys. Rev. Lett. **74**, 1751 (1995).

[32] A. La Porta, K. D. Eaton, and C. M. Surko, Phys. Rev. E **53**, 570 (1996).

[33] M. Lücke, W. Barten, and M. Kamps, Physica D **61**, 183 (1992).

[34] J. P. Gollub and A. R. McCarriar, Phys. Rev. A **26**, 3470 (1982).

[35] P. Kolodner and H. Williams, in *Nonlinear Evolution of Spatio-Temporal Structures in Dissipative Continous Systems*, edited by F. H. Busse and L. Kramer (Plenum, New York, 1990), pp. 73–91.

[36] K. D. Eaton *et al.*, Phys. Rev. A **43**, 7105 (1991).

[37] M. C. Cross and D. I. Meiron (unpublished).

[38] L. Ning, Y. Hu, R. Ecke, and G. Ahlers, Phys. Rev. Lett. **71**, 2216 (1993).

[39] P. Kolodner, D. Bensimon, and C. M. Surko, Phys. Rev. Lett. **60**, 1723 (1988).

[40] V. Croquette, Contemp. Phys. **30**, 113 (1989).